Chemical Engineering Journal 443 (2022) 136443

Contents lists available at ScienceDirect

Chemical Engineering Journal

journal homepage: www.elsevier.com/locate/cej

Amorphous calcium phosphate nanoparticles allow fingerprint detection via self-activated luminescence

Thales R. Machado [a,b,*], Jussara S. da Silva [b], Renata R. Miranda [a], Valtencir Zucolotto [a], Máximo S. Li [c], M. Valle Martínez de Yuso [d], Juan J. Guerrero-González [e], Ieda L.V. Rosa [b], Manuel Algarra [f,*], Elson Longo [b]

[a] GNANO - Nanomedicine and Nanotoxicology Group, Physics Institute of São Carlos, University of São Paulo, 13566-590 São Carlos, SP, Brazil
[b] CDMF - Center for the Development of Functional Materials, Federal University of São Carlos, 13565-905 São Carlos, SP, Brazil
[c] Physics Institute of São Carlos, University of São Paulo, São Carlos, SP, Brazil
[d] X-Ray Photoelectron Spectroscopy Lab, Central Service to Support Research Building (SCAI), University of Málaga, 29071 Málaga, Spain
[e] Policía Científica, Cuerpo Nacional de Policía, Málaga, Spain
[f] INAMAT²-Institute for Advanced Materials and Mathematics, Public University of Navarre, Campus de Arrosadia, 31006 Pamplona, Spain

ARTICLE INFO

Keywords:
Calcium phosphate
Nanoparticles
Luminescence
Defects
Forensics
Fingerprint
Imaging

ABSTRACT

Herein, stable activator-free photoluminescent nanoparticles based on amorphous calcium phosphate (ACP) were obtained for the first time, and their performance for latent fingerprint imaging was investigated. ACP nanoparticles with irregular rounded shape and diameters in 10–40 nm range were prepared by a rapid and simple chemical precipitation followed by heat treatment at 400 °C for 4 h. Notably, diffuse reflectance spectroscopy, photoluminescence excitation and emission measurements reveal a high density of localized energy states within the wide optical band gap of heat-treated ACP (E_g = 5.25–5.42 eV). This behavior allowed the excitation of ACP in near-ultraviolet region (λ_{exc} = 450 nm, 2.75 eV), leading to an intense defect-related broadband (490–890 nm) photoluminescence emission centered at 540 nm (2.30 eV), 50 times more intense than untreated nanoparticles. The effect of lattice shrinkage due to structural water elimination, the presence of ionic vacancies (V_{Ca} and V_O in PO_4^{3-}) and carbonate groups (CO_3^{2-}), on the luminescent properties of ACP were discussed in detail, as well as investigated after aqueous-mediated ACP crystallization into hydroxyapatite (HA). ACP nanoparticles were non-cytotoxic, as determined by MTT assay in Human Dermal Fibroblast neonatal (HDFn) cell line, with cell viabilities superior to 95% in all tested concentrations (20–320 μg/mL), after incubation for 24 and 48 h. Latent fingerprint images were obtained using the ACP nanoparticles under near-ultraviolet irradiation (λ_{exc} = 450 nm) in tweezers and LCD smartphone and successfully validated by the Integrated Automated Fingerprint Identification System used by Scientific Police in Spain. The present results evidenced that the new luminescent ACP nanoparticles are safe to be used and agree with the forensic requirements for future legal actions.

1. Introduction

Fingerprint analysis is one of the most explored biometric recognition approaches in forensic science for personal identification [1,2]. Usually, fingerprints left on surfaces cannot be observed by naked eyes, and a post processing step is often necessary, such as powder dusting, chemical fuming, and through typical formulations based on organic and fluorescent dyes [3–8]. Remarkably, since the pioneer use of zinc sulfide phosphor (ZnS) [9], the photoluminescent powders have been the most requested approach due to their resistance to photobleaching, and the ability to produce high resolution and sensitive fingermarks when illuminated under ultraviolet (UV) radiation.

Up to now, a variety of strategies based on nanotechnology have been developed to obtain fluorescent images of fingerprints with higher contrast by the improvement of the fluorescence intensity and stability of distinct materials. Many reports studied colloidal semiconductors such as quantum dots, which the main properties are strongly based in their particle size [10–15], rare earth nanoparticles (NPs), systems which increase the emission quantum yield due to *f* transitions in the shell environment [16–18], and noble metal NPs due to their inert

* Corresponding authors.
E-mail addresses: tmachado.quimica@gmail.com (T.R. Machado), manuel.algarra@unavarra.es (M. Algarra).

https://doi.org/10.1016/j.cej.2022.136443
Received 13 December 2021; Received in revised form 10 March 2022; Accepted 14 April 2022
Available online 16 April 2022
1385-8947/© 2022 Elsevier B.V. All rights reserved.

nature [19–21]. Recently, carbon NPs and carbon dots have emerged for this application [22–26].

Specifically, luminescent NPs comprising the calcium orthophosphate (CaP) family are interesting for forensic purposes. This is mainly due to their superior biodegradability, biocompatibility and easily scalable synthetic routes [27,28]. However, current research based on luminescent CaPs NPs, mainly focused on hydroxyapatite (HA) and amorphous calcium phosphates (ACPs), pointed towards other technological fields such as nanomedicine [29]. These NPs have received much attention mainly due to the high capacity to incorporate foreign ions, such as lanthanide ions, that allow the improvement of their luminescence properties [30].

On the other hand, Zollfrank *et al.,* [31] and Aronov *et al.,* [32,33] demonstrated the occurrence of intrinsic photoluminescence (PL) in HA and attributed this behavior to the presence of defect-related localized energy states. Since then, self-activated luminescence mechanisms in HA micro- and nanoparticles have been studied by several research groups [34–42], and were optimized for monitored drug delivery [43–47], bioimaging [48–50], biosensing [51,52], and secure information storage [53]. The main advantages of these strategies are that HA is made up of earth-abundant and relatively low-cost elements, where the achievement of intense luminescence avoids the need of doping with activator species. Also, the intrinsic luminescence was employed as a method to characterize HA-based photocatalysts [54], structural and compositional changes in bones [55,56], and in early caries detection [57].

In this study, the correlation between structural, optical, PL properties of ACP NPs were characterized for the first time and compared with those of HA NPs. ACP has significant structural resemblances with HA and is the first CaP phase precipitated from supersaturated aqueous solutions at the initial stages of the reaction between calcium and phosphate ions [58]. Hence, ACP can be prepared by faster and easier synthetic routes such as chemical precipitation. However, special attention is necessary to avoid its spontaneous crystallization in other CaPs. In the present work, ACP NPs were washed and recovered 1 min after precipitation. The post heat treatment step conducted at 400 °C plays a two-fold role. First, to increase ACP phase stability, a well know strategy to obtain stable powders at room temperature [59], and second, to improve the luminescent properties of ACP NPs, a crucial step observed for other CaPs [36,49]. Based on these results, this study allows the establishment of non-toxic and stable luminescent ACP NPs to be used for sensitive development of latent fingerprints.

2. Materials and methods

2.1. Materials

Calcium nitrate tetrahydrate ($Ca(NO_3)_2{\cdot}4H_2O$, 99%) was purchased from Sigma-Aldrich and di-ammonium phosphate ($(NH_4)_2HPO_4$, 98+%) from Strem Chemicals. Ammonium hydroxide, absolute ethanol, and acetone were purchased from Labsynth. Human Dermal Fibroblast neonatal (HDFn, catalog number C0045C) cell line was purchased from Thermo Fischer Scientific. Dulbecco's Modified Eagle's Medium (DMEM) and Fetal Bovine Serum (FBS) were purchased from Vitrocell. MTT (3-[4,5-dimethylthiazol-2-yl]-2,5-diphenyltetrazolium bromide) was purchased from Sigma-Aldrich, and dimethyl sulfoxide (DMSO) from Labsynth. All reagents were used as received without further purification.

2.2. Synthesis

The amorphous calcium phosphate ACP NPs were synthesized via an easy approach based on chemical precipitation. First, 50 mL of an aqueous phosphate solution (6 mmol of $(NH_4)_2HPO_4$, pH ~ 8.5) and 100 mL of an aqueous calcium solution (10 mmol, $Ca(NO_3)_2{\cdot}4H_2O$, pH ~ 6.8) were placed in separated flasks under vigorous stirring at room temperature. The pH values of both solutions were adjusted to ~ 10 by adding ammonium hydroxide. Then, the phosphate solution was added to calcium solution by one-batch step and the resulting mixture was stirred for 1 min. The solid product was recovered and washed thoroughly by centrifugation with water and acetone. The resulting slurry was dried at 60 °C for 4 h in air and is referred to as ACP sample. Then, the ACP powder was placed in alumina crucible and heat treated at 400 °C/4h in a programmable furnace at a heating rate of 10 °C/min. The sample was then naturally cooled to room temperature and is referred to as the ACP400 sample. Comparatively, we also allowed the crystallization of ACP in HA structure by increasing the aging step from 1 min to 24 h for a fraction of the resulting calcium and phosphate mixed solution described above. In this case, the solid product was recovered and washed several times with water and ethanol by centrifugation and dried over night at 80 °C. The HA sample was heat treated at 400 °C/4h in the same conditions than those used for ACP powder and is referred to as the HA400 sample.

2.3. Characterization

Transmission electron microscopy (TEM) was performed in a FEI TECNAI F20 (Netherlands) microscope operating at 200 kV. The prepared samples were structurally characterized by X-ray diffraction (XRD) in a Shimadzu XRD-6000 (Japan) diffractometer using CuK_α radiation ($\lambda = 0.154184$ nm). The data were collected using a step scan rate and step size of 0.2°/min and 0.02°, respectively. Fourier transform infrared (FTIR) spectroscopy was performed using a Nicolet iS50 spectrometer (Thermo Scientific, USA) operated in absorbance mode. The spectra were recorded at a resolution of 4 cm^{-1} over the wavenumber range of 400–4000 cm^{-1}. The peak asymmetry (ΔS) was estimated according to Equation (1) [60,61]:

$$\Delta S = (H_R - H_L)/(H_R + H_L) \quad (1)$$

where H_R and H_L are the right and left components of the full width at half maximum (FWHM) of the ν_3PO_4 and ν_4PO_4 bands.

X-ray photoelectron spectroscopy (XPS) studies were performed on a Physical Electronics PHI VersaProbe II spectrometer using monochromatic Al-K_α radiation (49.1 W, 15 kV and 1486.6 eV) for analyzing the core-level signals of the elements of interest with a hemispherical multichannel detector. The sample spectra were recorded with a constant pass energy value at 29.35 eV, using a 200 μm diameter circular analysis area. The XPS spectra obtained were analyzed using PHI SmartSoft software and processed using a MultiPak 9.3 package. The binding energy values were referenced to adventitious carbon C 1 *s* signal (284.8 eV). Shirley-type background and Gauss-Lorentz curves were used to determine the binding energies. Ultraviolet–visible (UV–Vis) spectroscopy was performed using a Shimadzu UV-2600 (Japan) spectrophotometer operated in diffuse-reflection mode. Excitation and emission PL spectra were acquired in a Horiba Jobin Yvon spectrofluorometer model Fluorolog-3, equipped with a 450 W Xe lamp as the excitation source. Signals were collected by a visible photodiode detector model PPD-850. All spectra were corrected by the lamp profile and detector response. PL spectroscopy was also conducted at room temperature by a Kimmon IK5451R-E HeCd laser ($\lambda_{exc} = 450$ nm) and using a Coherent Innova 200 K krypton laser (USA) ($\lambda_{exc} = 405$ nm) was used as the excitation sources.

2.4. Cytotoxicity assay

HDFn cells were used to investigate the potential cytotoxicity of ACP400 NPs in order to probe if the NPs are safe to be used for forensics purposes. Cells were cultured as a monolayer in DMEM supplemented with 10% v/v inactivated FBS, at 37 °C and 5% CO_2. For cell viability analysis, they were seeded onto a 96-well microplate at 2×10^4 cell/mL. After 24 h, the medium was replaced with fresh complete medium containing the NPs at different concentrations (0, 20, 40, 80, 160 and

320 μg/mL) and cells were incubated for 24 and 48 h. At the end of the exposure periods, HDFn cells were incubated with 0.5 mg/mL of MTT for 2 h, washed with phosphate-buffered saline and formazan was solubilized with 200 μL of DMSO. The absorbance was recorded at 570 nm using a SpectraMax M3 (Molecular Devices) plate reader. Three independent experiments with three replicates each were conducted. Data distribution was tested, and one-way analysis of variance (ANOVA) tests were performed, followed by Dunnett's post-test. Cytotoxicity was investigated by the comparison of the controls versus groups containing the NPs. p-values<0.05 were considered to be statistically significant.

2.5. Fingerprint imaging

Fingerprints recorded were analyzed to be validated by IAFIS system (3 M Cogent's Integrated Automated Fingerprint and Palm Print Identification System), a customizable software package that allows to perform a wide range of tasks for processing, editing, searching, retrieving, and storing fingerprint images and subject records used by Scientific Police in Spain. The acquisitions of the fluorescent fingerprints on the different surfaces were conducted by a Polilight PL10 (Rofin Australia). Excitation bands in NUV region (λ_{exc} = 350 and 450 nm) were used with yellow goggles (495 nm, edge wavelength) and orange goggles (edge wavelength 550 nm), respectively. The 450 nm excitation conditions produced superior images to NUV and further work was confined to this wavelength. The images of latent fingerprints were obtained using a Multi-zoom Nikon AZ-100 microscope and a Nikon-Digital Sight-5Mc, connected to the microscope by a computer, in which the pictures were stored and visualized by NIS-Elements software. The microscope was equipped with an epifluorescence system, in which the samples were illuminated by a mercury lamp (100 W) and a variety of available filter blocks (UV-2A: EX 330–380; DM 400; BA 420) were used.

3. Results and discussion

3.1. Morphology and long-range ordering (LRO) analysis

The morphological aspects of the as-prepared ACP and ACP400 samples were investigated by TEM, and the obtained images are displayed in Fig. 1a and 1b, respectively. Both samples are composed of chain-like NPs with irregular rounded shape and diameters ranging mainly from 10 to 40 nm. No significant difference of the morphological aspects was observed between ACP and ACP400 samples. The selected area electron diffraction (SAED) pattern of the ACP400 NPs shows a typical pattern of an amorphous material (inset Fig. 1b).

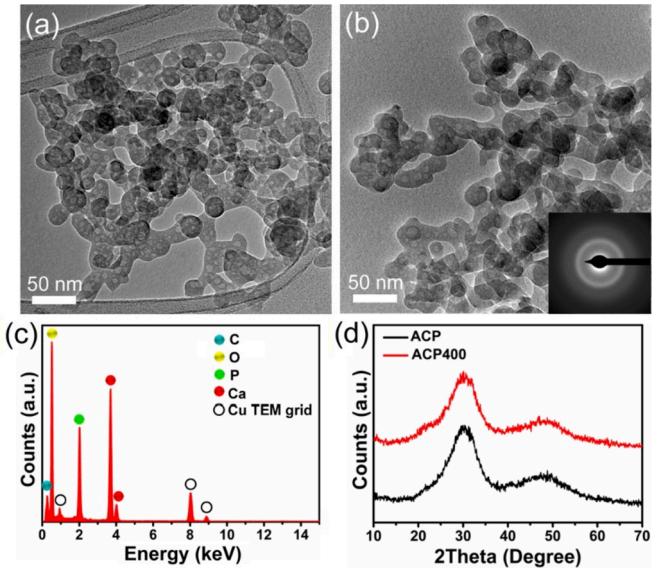

Fig. 1. TEM micrographs corresponding to (**a**) ACP and (**b**) ACP400 NPs (SAED pattern, inset), (**c**) EDS elemental analysis of ACP400 NPs, and (**d**) XRD patterns of prepared samples.

The chemical composition of ACP400 sample was evaluated by energy-dispersive X-ray Spectroscopy (EDS) (Fig. 1c), indicating the presence of Ca, P, and O elements, which consist of the main constituents of ACP structure. The presence of C can be mainly attributed to the carbon film of TEM grid. Ca/P molar ratio calculated by EDS analysis resulted in 1.43, which is close to but slightly lower than the value obtained for amorphous tricalcium phosphate (ATCP, Ca/P = 1.50), with general formula $Ca_3(PO_4)_2$. This was also found in a recent report for ACP samples synthesized in similar conditions [62]. Such decrease in Ca/P ratio is mostly related to the presence of acidic phosphate groups (HPO_4^{2-}) substituting PO_4^{3-} groups in the initial ACP NPs (see section 3.2), which is a well-known substitution in almost all ACP samples synthesized at pH < 11 [63]. These groups lowers the Ca/P ratio by generating calcium vacancies (V_{Ca}) in order to keep the electroneutrality in ACP structure [64].

Fig. 1d shows the XRD patterns of the ACP sample precipitated at room temperature. No discernible peaks of crystalline CaP phases were observed. Instead, the broad diffraction halo at $2\theta = 30°$ indicates that an amorphous phase which lack of LRO was preserved [65]. A poorly crystallized phase only appears when increasing the reaction time to 24 h (Figure S1a), which is related to the spontaneous conversion of ACP to calcium-deficient HA ($Ca_{10-x}(HPO_4)_x(PO_4)_{6-x}(OH)_{2-x}$ ($0 < x < 1$)) in the mother solution [58]. As also shown in Fig. 1d, the amorphous pattern of ACP sample persists after conducting the heat treatment at 400 °C for 4 h (ACP400 sample). The thermally induced crystallization of ACP sample was only observed when annealing it at higher temperatures (600 °C/4h), where peaks corresponding to the monoclinic α-tricalcium phosphate (α-TCP, α-$Ca_3(PO_4)_2$) phase were discernible (Figure S2). ACP is known to assume a hydrated TCP-resemble structure with the experimental conditions adopted [61,66], and posterior annealing procedures (T ≥ 600 °C) mainly lead to a solid state reordering of ACP in the crystalline TCP phases [67].

Considering that thermal stability is a critical parameter for long term use of ACP in practical applications, a further thermal aging treatment of ACP400 NPs was conducted at 80 °C/8h, based on a recent report [68]. No evidence of crystalline phases was observed after conducting this experiment (Figure S3), which assures the thermal stability of our ACP400 sample.

3.2. Short-range ordering (SRO) analysis

Fig. 2a shows the FTIR spectra obtained for ACP and ACP400 samples. The main vibrational modes of PO_4^{3-} groups are observed, including the asymmetric stretching mode of P–O bond (ν_3) in the 1300–900 cm^{-1} range, as well as the symmetric stretching mode of P–O bond (ν_1) appearing as a shoulder, and the bending mode of O–P–O bond (ν_4) in the 685–485 cm^{-1} range [69]. The broad and unsplited ν_3 and ν_4 modes herein observed are characteristic of ACP phase [70,71]. The presence of these vibrational bands evidences a certain degree of SRO of atomic groups in ACP and ACP400 NPs despite the lack of structural LRO detected by XRD.

A band with very weak intensity can be seen near 2300 cm^{-1} (Figure S4a) and is attributed to H–O(P) stretching mode of HPO_4^{2-} groups [72], confirming their presence in our ACP sample. The doublet between 1600 and 1375 cm^{-1} are assigned to the asymmetric stretching mode of C–O bond (ν_3) of CO_3^{2-} group, whereas the low intensity band centered at 871 cm^{-1} is related to the bending mode of O–C–O bond (ν_2) of this same group [69]. The presence of CO_3^{2-} impurity is typically associated to the precipitation of ACP under atmospheric conditions, which causes the solubilization of CO_2 from air followed by the incorporation of the resulting CO_3^{2-} groups in the amorphous material by the

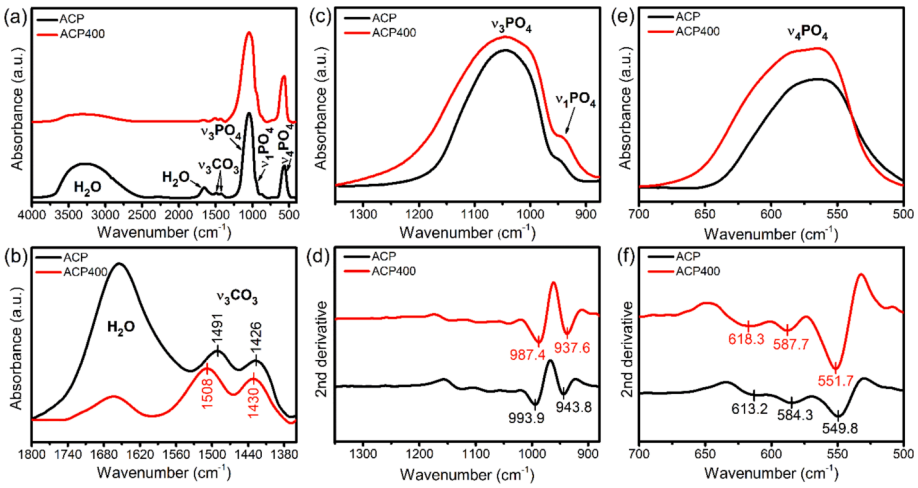

Fig. 2. **(a)** FTIR spectra of ACP and ACP400 samples, **(b)** magnified view of H_2O and ν_3CO_3 bands, **(c,e)** magnified views of ν_3/ν_1PO_4 and ν_4PO_4 bands, respectively, and **(d,f)** 2nd derivative spectra of ν_3/ν_1PO_4 and ν_4PO_4 bands, respectively.

substitution of PO_4^{3-} groups [73]. This substitution renders a global slightly increase in Ca/P molar ratio values, despite additional V_{Ca} vacancies are formed for charge balance implications. Based on the pertinent literature [62,63], we conclude that the Ca/P molar ratio of 1.43 found in ACP400 sample is a net result of the simultaneous presence of HPO_4^{2-} and CO_3^{2-} groups in precipitated ACP sample. Lastly, the bands associated with the vibrational modes of water molecules are observed in the range 3700–2500 cm^{-1} and at 1655 cm^{-1} [74].

As shown in Fig. 2a and 2b, a remarkable difference between FTIR spectra of ACP and ACP400 is the intensity of H_2O bands, which significantly decreases in the latter sample. *Eanes* [67] demonstrated that chemically precipitated ACP obtained at similar alkaline conditions (pH = 9.5–10) can retain ~ 15 wt% of water even after lyophilization. *Holmes and Beebe* [75] concluded that ~ 25% of this value corresponds to adsorbed water, whereas ~ 75% are tightly bounded water molecules inside ACP structure. More recently, *Uskoković et al.,* [61] corroborated with these seminal studies by obtaining similar water contents of 16.8 wt% in which 30% are adsorbed on ACP surface and 70% are inside the solid framework. Therefore, the dehydration observed in ACP400 sample of the present work are mainly associated to the irreversible elimination of these water molecules inside the ACP structure that occurs in the 25–400 °C temperature range and, in a less extend, to the reversible loss of adsorbed water [59,61,75].

As mentioned earlier, the presence of HPO_4^{2-} groups in ACP sample (Figure S4a) is typically detected in amorphous ACP phases [76,77], and is in agreement with the general formula of ACP, $Ca_xH_y(PO_4)_z{\cdot}nH_2O$ (n = 3—4.5) [58]. However, it disappeares upon heating (ACP400 sample) accompanied by the appearance of another weak band at ~ 730 cm^{-1} (Figure S4b). This new band is associated to $P_2O_7^{4-}$ formed by the condensation of HPO_4^{2-} groups according to the thermally-induced reaction $2HPO_4^{2-} \rightarrow P_2O_7^{4-} + H_2O\uparrow$ [72,78]. According to *Eanes* [67], even though there is an elimination of water from ACP lattice by this reaction, the water lost by heating is predominantly related to dehydration due to the low concentration of HPO_4^{2-} groups in the initial amorphous material.

As shown in Fig. 2c and 2e, a broadening in the PO_4^{3-} bands related to internal, short-range ν_3 and ν_4 vibrational modes when ACP NPs are heat treated at 400 °C is observed, reflecting in an increase of FWHM values from, respectively, 150 and 77 cm^{-1} for ACP NPs to 190 and 90 cm^{-1} for ACP400 NPs. These values represent a FWHM increase of 27% (ν_3) and 17% (ν_4) in ACP400. Moreover, the ν_3 and ν_4 PO_4^{3-} bands have become more asymmetrical in shape by the heating procedure, leading to a peak asymmetry (ΔS) of, respectively, 0.14 and 0.16 for ACP NPs to 0.21 and 0.23 for ACP400 NPs, which means a ΔS increase of 50% and 44%, respectively, for these bands. As stated by *Uskoković* [60], these data can be interpreted as a decrease in SRO into PO_4^{3-} groups of ACP400 NPs with a consequent larger absorption of varied frequencies although temperature-related structural changes usually tend to lead higher degrees of structural ordering in materials. As previously discussed, an important loss of tightly bounded water occurred in ACP400 (Fig. 2a and 2b). This liberation is known to lead to an overall contraction in ACP lattice to remove empty spaces [60]. Hence, the structural shrinkage significantly increases the lattice strain and led to even more distorted environments around the PO_4^{3-} clusters, reflecting in the asymmetrical broadening of ν_3 and ν_4 PO_4^{3-} modes due to fluctuations in P–O bonds length and in the O–P–O bond angles inside the PO_4^{3-} structure.

A further evidence of structural changes in the PO_4^{3-} groups and their neighborhoods by annealing at 400 °C is the redshift of one observable component for the triply degenerated asymmetric stretching mode (ν_3) from 994 to 988 cm^{-1}, the redshift of the non-degenerated symmetric stretching mode (ν_1) from 943 to 937 cm^{-1} and, in opposite, the blueshift of all components of the triply degenerated bending mode (ν_4) from 612, 585, 550 to 618, 588, 553 cm^{-1}, respectively, as analyzed by the second-derivative plots (Fig. 2d and 2f). This effect is associated to stronger interactions of PO_4^{3-} groups with the near-neighbor atoms into the ACP shrunken lattice that occurs at temperatures below the amorphous-to-crystalline phase transition [60].

In ν_3 bands of CO_3^{2-} groups (Fig. 2b) important features are sensed after the heat treatment procedure: **(i)** a slight decrease in intensity of the doublet, which is associated to a partial sublimation of this impurity as CO_2 at 400 °C [60], **(ii)** a blueshift of the doublet from 1491 and 1426 cm^{-1} to 1508 and 1430 cm^{-1}, and **(iii)** a slight increased separation of the doublet from 65 to 78 cm^{-1}. These last two characteristics of ν_3 modes are sensitive to the structural location of CO_3^{2-} impurities in CaPs [78] and are susceptible to changes in the amount of hydration water into lattices with surrounds that strongly interact with these groups [79–82]. In this sense, the present results indicate that the remaining CO_3^{2-} groups were influenced by the compositional and organizational changes at the surroundings due to the water loss and lattice contraction, leading to different *stereo*-chemistries for CO_3^{2-} groups with more energetic C–O bonds.

3.3. Surface analysis

The surface chemical composition of ACP400 sample is based on O 1*s* (53.9 at.%),

C 1*s* (17.2 at.%), P 2*p* (12.8 at.%), and Ca 2*p* (16.1 at.%), as detected on the survey scan (Fig. 3a). Basically, the XPS analysis showed that the

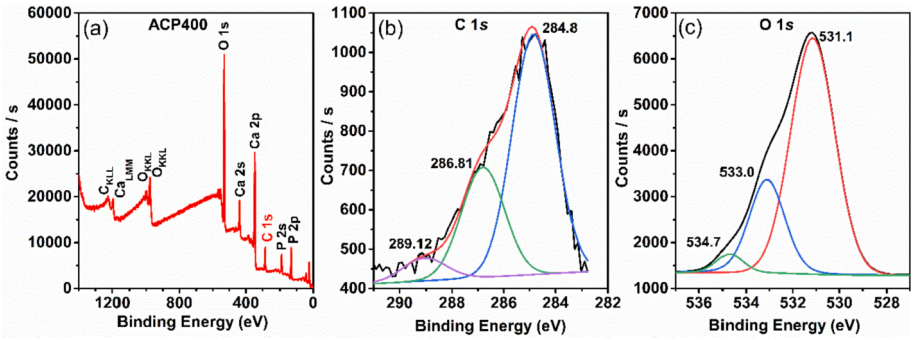

Fig. 3. (**a**) Survey XPS spectrum of ACP400 NPs. High-resolution XPS spectra of (**b**) C 1 *s* and (**c**) O 1 *s*.

most key information was found in the C 1 *s* signal (Fig. 3b), which can be deconvoluted in three main contributions. A main peak at 284.8 eV is mostly attributed to surface hydrocarbon chains after heat treatment at 400 °C (C–C/C–H bonds); the further two shoulders at 286.8 and 289.1 eV are assigned to C–O and C = O (carbonyl)/O = C–O$^-$ (carboxyl bonds), respectively, which are attributed to CO_3^{2-} on the surface of ACP400 NPs [83]. Moreover, O 1 *s* was deconvoluted in three main contributions at 531.0 (C = O), 533.1 (C–O/P = O) and 534.7 eV (P–O) [84] (Fig. 3c). These results indicate the presence of graphitized carbon and CO_3^{2-} groups from ACP. The other peaks related to P 2*p* do not show relevant inputs. The signal attributed to the PO_4^{3-} component showed a single peak, indicating that all the P atoms have an equivalent environment.

3.4. Optical properties

In a semiconductor, the optical band gap energy (E_g) describes the energy needed to excite an electron from the valence band (BV) to the conduction band (CB). E_g can be estimated by the Tauc's method according to Equation (2):

$$(\alpha h\nu)^{1/n} = A(h\nu - E_g) \quad (2)$$

where α is the absorption coefficient, hν is the incident photon energy, A is a constant depending on the transition probability, while n is equal to 1/2 or 2 for direct and indirect transition bandgaps, respectively [85]. The diffuse reflectance spectroscopy is often used to determine the E_g value, and Figure S5 illustrates the reflectance spectra obtained for ACP and ACP400 samples. The Kulbelka-Munk function, $F(R_\infty)$, can be derived from these spectra as given by Equation (3):

$$F(R_\infty) = \frac{(1-R_\infty)^2}{2R_\infty} = \frac{\alpha}{s} \quad (3)$$

where R_∞ is the reflectance and *s* is the scattering coefficient. $F(R_\infty)$ is proportional to α if s is assumed to be wavelength independent and can substitute α in Equation (3) [86]. The plot of $[F(R_\infty)h\nu]^{1/n}$ vs. hν leads to the Tauc's plot, and the E_g value is obtained by fitting and extrapolating the linear portion of the plot to the energy axis. Fig. 4a and 4b show the Tauc's plots of our samples considering the previous approach. Additionally, we also used a linear fit as the abscissa (blue dotted line) for each spectrum presenting significant sub-bandgap absorption. According to *Makuła et al.*, [87], the use of this baseline method leads to more accurate estimation of E_g value by the intersection of the two fitted lines.

Herein, two important insights can be highlighted. First, the E_g values calculated for both ACP (E_g = 5.53 and 5.42 eV for n = 1/2 and 2, respectively) and ACP400 samples (E_g = 5.22 and 5.25 eV for n = 1/2 and 2, respectively) are closely related to those found in crystalline CaPs, including α-TCP (E_g = 4.89 eV) and β-TCP (E_g = 5.25 eV) [88], with direct bandgap transitions, as well as HA (E_g = 4.51—5.78 eV) [36,89–93] and Ca-dHA (E_g = 5.67 eV) [94], with indirect bandgap transitions. The band structures of these materials are mainly composed by overlapped P 3 *s*, P 3*p* and O 2*p* orbitals from covalent PO_4^{3-} groups at the upper VB, with minor contributions of Ca 4 *s* and 3*d* components due to ionic interactions of Ca with O from neighboring PO_4^{3-} groups, as well as components from OH groups in the case of HA and Ca-dHA, whereas the bottom of CB is mainly composed by Ca 3*d* components [88–91,94]. Since SRO is the key feature for the electronic properties of a solid [85], we can assume that the close E_g values between our ACP samples and those found for other CaPs emerge from the structural similarities at short-range between the amorphous and crystalline phases, leading to comparable band structures.

Second, a decrease in E_g from 5.53 to 5.42 eV (Fig. 4a) is observed by conducting the heat treatment at 400 °C/4h. This decrease is accompanied by an increment in tailing of band states extending within the forbidden gap. In poorly crystalline and amorphous materials, the presence of these tails of energy states instead of sharp band-edge absorptions is characteristic of a broad distribution of defect levels which vary upon the degree of lattice disorderliness [95]. The tail absorption exponentially depends on photon energy, and the plot of $\ln[F(R_\infty)]$ vs. hν can be used to calculate the Urbach energy (E_u) or Urbach tail width

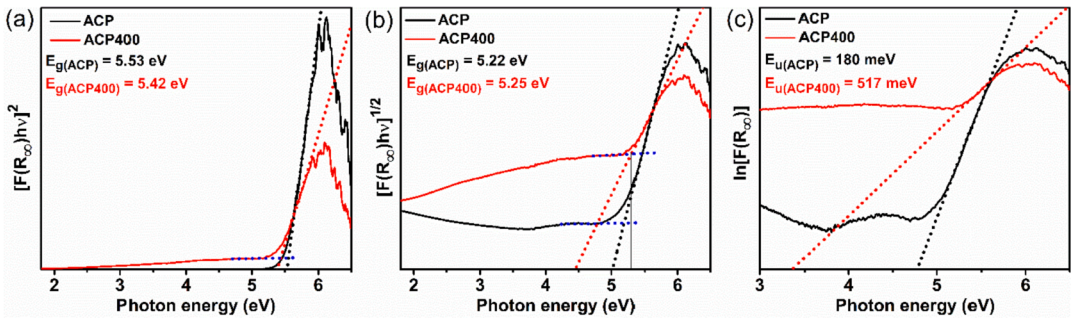

Fig. 4. E_g and E_u energies for ACP and ACP400 samples. Tauc's plots for (**a**) direct transition (n = 1/2) and (**b**) indirect transition (n = 2). (**c**) Plots of $\ln[F(R_\infty)]$ vs. photon energy.

by the slope of the straight line obtained in this plot. In our case, E_u = 180 and 517 meV for ACP and ACP400, respectively, as shown in Fig. 4c. The E_g decrease and E_u increase after the heat treatment step could be attributed to an increment in lattice disorder (lower degree of SRO) for ACP400 compared to ACP sample, due to the wider deviations of bond lengths and bond angles from the ideal values, as was also observed by FTIR data (section 3.2).

3.5. PL properties

Fig. 5a and 5b show the excitation spectra of ACP and ACP400 NPs recorded by monitoring the main PL emission at λ_{em} = 530 and 540 nm, respectively. A broad and intense band centered at 243 nm (5.10 eV) is sensed in both samples and can be attributed to the excitation departing from band states and localized tail states. The inset of each figure shows a magnified view over a selected wavelength region (260–520 nm). A weak but clear band extending up to 500 nm with maxima at 370 nm (3.35 eV) and 398 nm (3.12 eV) is observed in ACP NPs. On the other hand, this region in ACP400 NPs is composed by a weak band in the 300–375 nm range with maximum at 317 nm (3.91 eV), as well as by a band in the 400–520 nm range with maxima at 456 nm (2.72 eV) and 484 nm (2.56 eV). As the excitation energies are much lower than E_g values in both samples, these bands can be attributed to excitation involving localized energy states from point defects in ACP structure, as were also observed in other materials with similar spectral features [96]. These data evidence that there is an important reorganization of the energy levels within the band gap in ACP by conducting the thermal treatment.

Fig. 5c shows the PL emission spectra of ACP and ACP400 NPs recorded at λ_{exc} = 450 nm. The excitation wavelength was selected to resemble the one employed in fingerprint analysis. Both samples exhibited broadband emission profiles originated from radiative recombination of electron-hole pairs (e^-–h^+) through pathways which can encompass extended energy states as well as countless localized energy states. Considering that both the excitation and emission wavelengths have significantly lower energies than the Eg calculated, the contribution of band-to-band transitions between extended energy states is negligible. The emission band of ACP NPs ranges from 490 to 740 nm and reaches it maximum of intensity at 530 nm (2.34 eV), whereas for ACP400 NPs the emission band is broader and falls into the 490–800 nm range with maximum at 540 nm (2.30 eV). Another remarkable feature observed in PL spectra is the expressive increase in intensity by at least 50 times after the heat treatment of the NPs at 400 °C.

To evaluate the effect of distinct excitation sources on the PL properties of the prepared samples, the emission spectra were also recorded using the 442 nm line of HeCd laser (Fig. 5d). Only a minor change on the inclination of the bands at shorter wavelengths is sensed due to the distinct configuration of the optical filters employed, as well as a slight increase in the resolution of the emission bands when compared to the spectra acquired via spectrofluorometer, i.e., the maxima of the bands are now centered at 521 and 540 nm for ACP NPs and at 540 and 569 nm for ACP400 NPs. This feature is mainly related to the narrower excitation line of the laser source.

The distinct characteristics observed between the emission profiles of ACP and ACP400 NPs (Fig. 5c and 5d) influenced the color of PL observed, mainly associated to the increase on the relative contribution of radiative emissions at longer wavelengths in ACP400 sample. Fig. 5e shows the Comission Internationale de l'Éclairage (CIE) chromaticity diagram. The CIE coordinates shifted from × = 0.38/0.37 and y = 0.57/0.52 for ACP to × = 0.53/0.52 and y = 0.45/0.44 for ACP400 (spectrofluorometer/laser), corresponding to green-yellow and yellow-orange regions, respectively. Also, the close-related CIE coordinates for both excitation sources confirm the reproducibility of the emission profiles using distinct luminescence techniques and indicate that the color of the PL observed was not considerably affected. The broadening and red shift of the emission band with a consequent change in emission color observed in Fig. 5e is often associated to a decrease in structural ordering in materials [97–99], confirming that ACP400 exhibits a higher degree of lattice disorder than the ACP sample induced by the heat treatment procedure employed in this study.

3.6. Hypotheses for PL properties of ACP

The nature of the PL properties in ACP are not completely clear yet, but according to this study the determining factor is the presence of localized energy states due to order–disorder effects. In the last years, the electronic structure and PL properties of HA were studied due to its potential applications in optical devices and in nanomedicine [29], but no previous literature was found concerning the ACP structure. In this sense, to better elucidate the nature of PL emissions in the amorphous NPs, we measured the emission spectra of ACP after allowing its

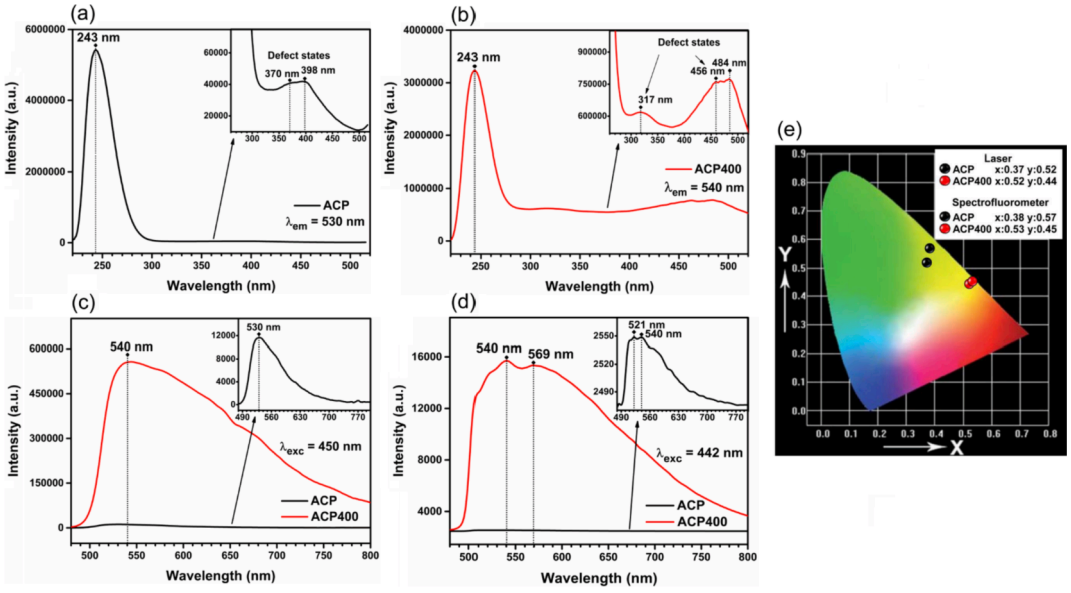

Fig. 5. (a,b) PL excitation spectra of ACP and ACP NPs, respectively. PL emission spectra obtained by a (c) spectrofluorometer (λ_{exc} = 450 nm), and (d) HeCd laser (λ_{exc} = 442 nm). (e) Calculated CIE chromaticity coordinates from the PL emission spectra.

conversion into calcium-deficient HA, and the results are illustrated in Fig. 6a-c. In this case, we excited our samples at λ_{exc} = 405 nm with a higher energy laser source to allow the comparison of the results with those of former published studies [36,39]. Interestingly, both amorphous (ACP) and poorly crystallized (HA) samples presented broad-bands with comparable profiles. A plausible reason for the similar PL emission spectra after ACP → HA transition could be explained based on their structures at short-range.

ACP NPs were proposed to exhibit SRO due to the presence of randomly packed $Ca_9(PO_4)_6$ units with an average size of 9.5 Å (Posner's clusters) [65] which, in turn, resemble a spatial subset of Ca^{2+} and PO_4^{3-} in HA unit cell [58]. The mechanisms governing the ACP → HA transition are not yet fully understood, but it is well-accepted that there is key role of aqueous environments for the occurrence of solid-state reorganization, dissolution/reprecipitation, self-assembly aggregation and partial dissolution-aggregation mechanisms [77,100]. More to the point, several studies experimentally confirmed the existence of the proposed Posner's clusters and that these basic pre-nucleation clusters are conserved during ACP → HA transformation [77,101,102]. As to say, although there is a LRO increase in the ACP → HA phase transition with the presence of translational symmetry and stricter distribution of environments in HA structure, both materials possesses similarities at short and medium range spatial organization of atomic groups [58,60], which could result in comparable atomic interactions and electronic structures (see section 3.4), as was also observed in other amorphous/crystalline semiconductors [85].

Considering the previous discussion, it is also plausible that the order–disorder effects which govern the PL for chemically precipitated ACP and HA samples have similar nature. In HA, the PL emission was proposed to arise mainly from perturbations of Ca and PO_4 electronic densities which led to new acceptor and donor-like localized states inside the band gap [37]. These states arise from the VB and CB, respectively, with Ca 3*p*, Ca 4 *s*, P 3 *s*, P 3*p*, O *2 s*, and O 2*p* character [103]. This lattice disorder was mainly attributed to ionic vacancies (V_{Ca}, V_H, V_{OH}, and V_O in PO_4^{3-} groups) and to distortions in the bond's lengths and angles of the structural coordination clusters [35,37,40,103,104]. Some reports also concluded that CO_3^{2-} impurity and the defects associated to its stabilization in HA lattice could contribute to the defect-related PL emission [39,45,49].

In ACP NPs, perturbations in Ca and PO_4 electronic densities could occur due to fluctuations in Ca–O and P–O bonds length and O–Ca–O and O–P–O bonds angle (Fig. 2), which is a characteristic of ACP structure, originating the localized tail states (Fig. 4). Besides, *Bystrov et al.,* [54] evidenced by DFT calculations of HA that V_O vacancies in PO_4 groups lead to fully occupied peaks at 344 nm (3.60 eV eV), 358 nm (3.47 eV), and 366 nm (3.39 eV) bellow the CB. *Huerta et al.,* [40] experimentally proposed that this level occurs at 373 nm (3.32 eV). In this study, we propose that the defect-related excitation band centered at 370 nm (3.35 eV) and 398 nm (3.10 eV) of ACP NPs mainly stems from energy states associated to V_O in PO_4^{3-}. Hence, the PL emission (Fig. 5c) originates by excited electrons departing from this band, which subsequently follow a complex multistep decay through radiative and non-radiative pathways involving distinct extended and/or localized levels. The latter levels could arise from tail states and from defect states due to Vo in PO_4^{3-}, V_{Ca}, as well as from CO_3^{2-} impurity and the defects associated to its stabilization in ACP lattice.

The heat treatment at 400 °C of ACP lead to a new excitation band in 400–520 nm range, which is closer to the excitation wavelength used (450 nm), rendering improved PL emissions compared to as-synthesized ACP NPs. We believe that this new band has a great contribution from temperature-induced changes of CO_3^{2-} impurity trapped in ACP400 NPs and their environments. *Zollfrank et al.,* [31] proposed that annealing biomimetic HA at 400 °C enhance the presence of self-trapped electrons in carbonates (CO_3^{3-}) giving rise to improved PL emission. Our recent studies [36,49] with HA corroborated by the investigations conducted by *Gonzalez et al.,* [39] also concluded that CO_3^{2-} impurities could play important role on the PL emission observed in NPs heated at 350–450 °C. In the case of ACP structure, the SRO modifications in CO_3^{2-} group observed by FTIR spectrum of ACP400 NPs (Fig. 2b) supports the aforementioned arguments, since (1) this group become richer in electronic density after annealing due to changes of interaction with surrounding crystal field, and (2) CO_3^{2-} environment become more anisotropic (i.e., greater C–O bonds distortions). Hence, the changes in bond character of CO_3^{2-} group and in its surroundings, as well as the pronounced impact of the short-range disorder on CO_3^{2-} internal arrangement contribute to the improved excitation capability of ACP400 NPs in higher wavelength regions than ACP NPs.

Furthermore, *Zhang et al.,* [34] related the role of $CO_2^{\dot{A}\cdot-}$ radicals for the PL observed in HA. *Jiang et al.,* [105] more recently observed that these impurities are in fact N-rich carbon dots present on the surface and inside of HA NPs acting as luminescent centers, which was further corroborate by other studies [50,53]. However, no clear signs of carbon dots were observed herein. A main difference is that these authors used significant amounts of citrate precursors which is known to decompose in carbon dots by hydrothermal treatment. By XPS (section 3.3), we observed the presence of surface hydrocarbon chains adsorbed on the surface of ACP400 NPs. However, the substantial contribution of adventitious carbon to the PL emission can be discarded, since it is known that a similar adsorption capability is retained on the NPs after ACP → HA transition [106]. Nevertheless, as shown in Fig. 6b, the emission intensity of HA400 is 5 times less intense compared to ACP400 NPs.

Lattice water elimination when ACP is heat treated up to 400 °C is then a crucial mechanism to be considered to the improved PL properties of ACP400. Hydration water was previously proposed by *Posner* and *Betts* [65] to occupy interstitial positions between the $Ca_9(PO_4)_6$ clusters composing the ACP NPs. *Termine* and *Lundy* [69] argued that H_2O

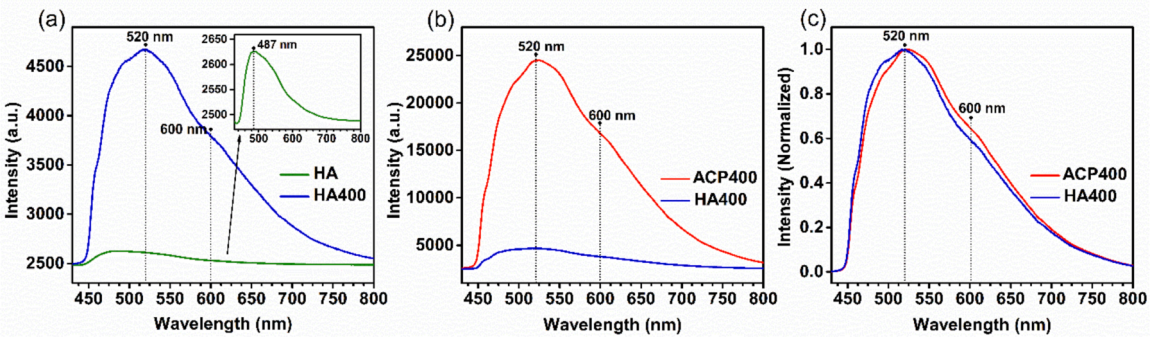

Fig. 6. PL emission spectra (λ_{exc} = 405 nm) of (**a**) chemically precipitated HA obtained after ripening for 24 h and after conducting the heat treatment step at 400 °C, (**b**) PL spectra of ACP and HA heat treated at 400 °C, and (**c**) normalized PL spectra of ACP and HA heat treated at 400 °C.

molecules contribute with ACP coordination structure, and *Du et al.,* [107] proposed that this water is coordinated with Ca atoms of the outer shell of Posner's subunits. Moreover, *Uskoković et al.,* [61] stated that before annealing, the water-rich ACP lattice possesses a large amount of hydrogen bonding between H_2O molecules and PO_4^{3-} groups. *Yasar et al.,* [62] concluded by NMR measurements that there are close $H_2O\cdots CO_3^{2-}$ and $H_2O\cdots PO_4^{3-}$ contacts in the ACP-particle interior.

Due to this active bonding of H_2O molecules with their surroundings, it could be expected that their removal influences the bond character of the remaining atomic groups in ACP lattice, as was observed for the strong polarizable PO_4^{3-} and CO_3^{2-} groups. Moreover, as evidenced by *Uskoković* [60], an important shrinkage of the ACP lattice occurs by heating up to 400 °C in order to close the voids resultant from the release of water. This contraction with consequent increase in lattice strain and decrease in SRO of ACP400 lattice, observable as shifts and broadening of bands related to PO_4^{3-} and CO_3^{2-} vibrational modes in FTIR (Fig. 2d and 2f), could intensify the electronic interactions between neighbor atomic groups with significant increase in PL emission intensity. This is because of the enhancement in oscillator strength and the consequent higher probability of radiative electronic transitions that takes place, as well as the increase in the density of localized states within the forbidden zone.

In our previous publication [36], we also observed an important contraction in crystalline lattice of HA NPs up to 400 °C/4h after the elimination of impurities with consequent increase in PL emission. This difference in PL intensity of ACP400 and HA400 materials could result mainly from the distinct characteristics of hydration water in their lattices. When the ACP → HA transition takes place in aqueous media, the concentration of hydration water is known to be reduced from ~ 15 wt% for ACP to values below 3.5 wt% for HA [49,67] and the activation energy (E_a) for dehydration is also reduced from 23.6 kJ/mol for ACP to 12.5 kJ/mol^{-1} for HA [61]. Thereby, ACP possess higher concentration of hydration water molecules which are more tightly bounded in its amorphous lattice than in HA one. These characteristics imply a less pronounced structural impact at short-range in HA lattice than in ACP by the loss of water, leading to lower density of similar localized energy states and/or probability of radiative electronic transitions in HA400 NPs.

The experimental data obtained in this study evidenced that the heat treatment at intermediates temperatures close to 400 °C is an important step in order to obtain CaPs with improved PL properties. Pivotal role are the concomitant impurity reactions (H_2O and CO_3^{2-}) that takes place in ACP lattice during the temperature-induced structural reorganization. These results could open venues toward new optical devices using ACP400 NPs with stable structural and PL properties, as demonstrated by the thermal stability probe (see section 3.1 and Figure S3) and the long-term stability analysis conducted after 10 months by collecting the FTIR and PL spectra (Figure S6), where no significant changes were observed in comparison with the as-synthesized ACP400 sample.

Although the results in Fig. 6b evidenced that ACP400 sample has a higher PL emission intensity than HA400 sample, the use of HA NPs for forensic purposes is not discarded, since intense emission is observable in heat-treated HA even with the naked eye [36]. Furthermore, the PL properties of as-synthesized or heat treated HA and fluoridated-HA can be optimized through doping with activator ions [93,108–111], or with foreign ions that induce tunable amounts of defects, leading to an enhancement of the self-activated PL emissions in HA [112]. These strategies could also be used to obtain luminescent HA NPs aiming fingerprint imaging applications.

3.7. Cytotoxicity assay

The MTT assay was used to evaluate the cytotoxicity of ACP400 NPs on HDFn cells, and the results are illustrated in Fig. 7. After incubation with ACP400 NPs for 24 h and 48 h, HDFn cells viability was superior to

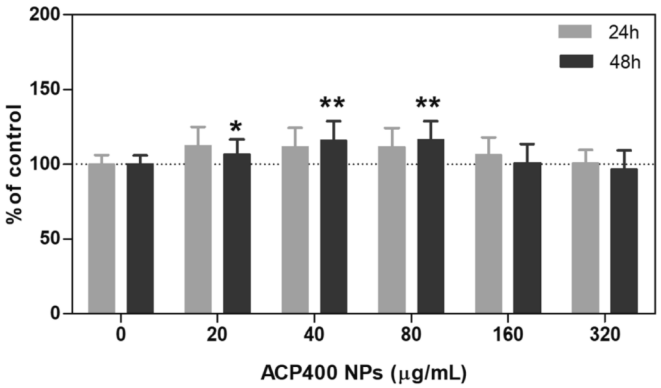

Fig. 7. Cell viability analysis of HDFn cells after incubation with increasing concentrations of ACP400 NPs, for 24 and 48 h. Mean ± SD of three independent experiments in triplicate. Asterisks indicate difference in comparison to the control (* $p < 0.5$ and **$p < 0.01$).

95% in all NPs tested concentrations (from 20 to 320 μg/mL). The statistical analysis revealed that there is no significant difference between the control and APC400 NPs-treated cells, except for the ones containing 20 μg/mL (24 h), 40 and 80 μg/mL (48 h) of NPs, in which a slight increase in cell viability occurred. These results are in accordance with the superior cell viability found for luminescent HA NPs exposed to HDFn cells in similar conditions [49]. Hence, the low cytotoxicity observed for the luminescent ACP400 NPs evidences the potential of this CaP to be used as safe material for forensics purposes.

3.8. Application for fingerprint imaging

The feasibility of ACP400 NP for fingerprint imaging was probed in a pair of surfaces from utensils of daily use, and the results are shown in Fig. 8. Under NUV light, the development of fingerprints was successfully obtained by the pale fluorescent yellow color from ACP400 NPs. Moreover, a more accurate image was observed in the stainless-steel tweezers (Fig. 8a) than in the polymeric material on the screen smart surface (Fig. 8d). This allowed us to obtain clear and well resolved ridges, bifurcations, and lakes.

To evaluate the viability of AC400 NPs as an alternative system for latent fingerprint imaging, the digitalized images obtained in the stainless-steel tweezers (Fig. 8b) and in the polymeric material (Fig. 8e) were compared with those acquired by the standard procedure in the entrance of the Police database based on ink fingerprints (Fig. 8c and 8f). After the input on the Integrated Automated Fingerprint Identification System (IAFIS), a process using a computer to match fingerprints against a database of known fingerprints. Our analysis compared the different traits in the obtained fingerprint founding 14 matches. These results agree with the forensic requirements to be take in account for future legal actions.

The mechanism for imaging fingerprints could be explained by the electrostatic interactions of the negative surface due to O = P-O functional groups (mainly phosphate) and basic proteins of the secretion components, as previously reported [86]. The analyst compares minutiae characteristics and locations to determine if they match. The analysis showed the satisfactory performance of ACP400 when used for latent fingerprint detection. ACP400 NPs are fluorescent and non-toxic, and the images obtained are more shinny that those obtained with ink. The proposed method offers a certain advantage to the methods that are currently used by the Scientific Police, such as those based on non fluorescent magnetic nanoparticles [113], dyes [8], ink [114], and metal oxides for fingerprint detection [115]. Furthermore, as highly fluorescent systems, it was previously proposed the application of QDs [12] but, due to their low biocompatibility, carbon dots were brought to light [22,24], and here we suggest the ACP400 NPs.

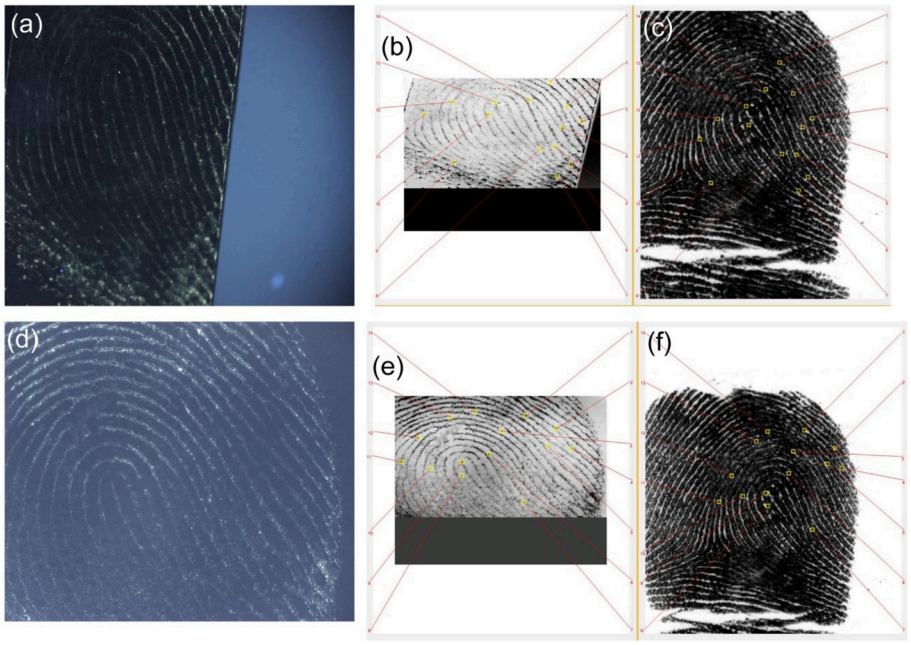

Fig. 8. Latent fingerprint images based on ACP400 NPs obtained under UV irradiation in (**a**) tweezers and (**b**) LCD smartphone. (**c,d**) Digitalized images of UV-exposed surfaces containing ACP400 NPs. (**e,f**) Digitalized images of the fingerprints obtained from the standard procedure by ink processing. Data analysis was conducted using IAFIS system.

4. Conclusions

In summary, intrinsically photoluminescent, biocompatible, and stable nanoparticles based on chemically precipitated ACP heat-treated at 400 °C for 4 h were successfully synthesized. SAED, XRD and FTIR results confirmed that the amorphous pattern was present after the heat treatment, but also stemmed a significant decrease in structural short-range ordering, observed in FTIR as a broadening of the PO_4^{3-} bands and an increase in peak asymmetry. Furthermore, the stereochemistry of the structural CO_3^{2-} groups present into the ACP amorphous lattice was also significantly affected. These structural changes occur due to the shrinkage of ACP lattice as an effect of hydration water elimination at 400 °C. The aforementioned phenomena, together with V_{Ca} and V_O vacancy in PO_4^{3-}, were attributed to be the possible causes of the high density of localized tail and defect states into the forbidden band gap of heat-treated ACP, detected by diffuse reflectance via UV–Vis spectroscopy, and by photoluminescence excitation and emission measurements.

When excited at $\lambda_{exc} = 450$ nm, the photoluminescence emission of heat-treated ACP nanoparticles is 50 times greater comparing to freshly precipitated ACP and consists of a broadband defect-related emission profile centered at 540 nm and encompassing most part of visible region (490–800 nm). The emission possesses a yellowish color, as was determined by CIE chromaticity coordinates using distinct excitation sources (x = 0.53; y = 0.45, spectrofluorometer, and × = 0.52; y = 0.44, HeCd laser). The structural and luminescent features remained almost unchanged after 10 months, demonstrating the superior stability of the heat-treated nanoparticles. When used for fingerprint imaging, the bright yellow patterns of unique features from ACP luminescence were well observed on the surface of tweezers and LCD smartphone under NUV irradiation ($\lambda_{exc} = 450$ nm). These nanoparticles presented interactions with biomolecules and those interaction led to specific fluorescent patterns. Moreover, the non-cytotoxic response of ACP observed by MTT assay evidences the potential of this calcium orthophosphate to be used as safe material for forensics purposes.

Declaration of Competing Interest

The authors declare that they have no known competing financial interests or personal relationships that could have appeared to influence the work reported in this paper.

Acknowledgments

The authors acknowledge the financial support of the following agencies: Conselho Nacional de Desenvolvimento Científico e Tecnológico (CNPq, Grants 164373/2020-9 and 141964/2018-9), and Fundação de Amparo à Pesquisa do Estado de São Paulo (FAPESP, Grant 2013/07296-2). MA thanks to COST Action 16101 and Spanish Ministry of Science and Innovation (project RTI2018-099668-B-C22). Special thanks to Prof. Andrea Simone Stucchi de Camargo Alvarez Bernardez and Dr. Leonnam Gotardo Merizio for the support with photoluminescence spectroscopy measurements and Prof. Waldir Avansi for the support with UV-Vis spectroscopy.

Appendix A. Supplementary data

Supplementary data to this article can be found online at https://doi.org/10.1016/j.cej.2022.136443.

References

[1] D.R. Ashbaugh, Quantitativa-qualitative friction ridge analysis: An introduction to basic and advanced ridgeology, CRC Press, Boca Raton, Florida, 1999.
[2] A.K. Jain, A. Ross, S. Prabhakar, An Introduction to Biometric Recognition, IEEE Trans. Circuits Syst. Video Technol. 14 (2004) 4–20, https://doi.org/10.1109/TCSVT.2003.818349.
[3] D.A. Wilkinson, A. Misner, A comparison of thenoyl europium chelate with ardrox and rhodamine 6G for fluorescent detection of cyanoacrylate prints, J. Forensic Identif. 44 (1994) 387–407.
[4] G. Sodhi, J. Kaur, R.K. Garg, Fingerprint powder formulations based on organic, fluorescent dyes, J. Forensic Identif. 54 (2004) 4–8.
[5] D.S. Bhagat, P.B. Chavan, W.B. Gurnule, S.K. Shejul, I.V. Suryawanshi, Efficacy of synthesized azo dye for development of latent fingerprints on Non-porous and wet surfaces, Mater. Today Proc. 29 (2020) 1223–1228, https://doi.org/10.1016/j.matpr.2020.05.480.
[6] H.L. Barros, L. Tavares, V. Stefani, Dye-doped starch microparticles as a novel fluorescent agent for the visualization of latent fingermarks on porous and non-

porous substrates, Forensic Chem. 20 (2020), 100264, https://doi.org/10.1016/j.forc.2020.100264.
[7] M. Chen, R. Chen, Y. Shi, J. Wang, Y. Cheng, Y. Li, X. Gao, Y. Yan, J.Z. Sun, A. Qin, R.T.K. Kwok, J.W.Y. Lam, B.Z. Tang, Malonitrile-Functionalized Tetraphenylpyrazine: Aggregation-Induced Emission, Ratiometric Detection of Hydrogen Sulfide, and Mechanochromism, Adv. Funct. Mater. 28 (2018) 1704689, https://doi.org/10.1002/adfm.201704689.
[8] C. Yuan, M. Li, M. Wang, X. Zhang, Z. Yin, K. Song, Z. Zhang, Sensitive development of latent fingerprints using Rhodamine B-diatomaceous earth composites and principle of efficient image enhancement behind their fluorescence characteristics, Chem. Eng. J. 383 (2020), 123076, https://doi.org/10.1016/j.cej.2019.123076.
[9] M.J. Choi, K.E. McBean, P.H.R. Ng, A.M. McDonagh, P.J. Maynard, C. Lennard, C. Roux, An evaluation of nanostructured zinc oxide as a fluorescent powder for fingerprint detection, J. Mater. Sci. 43 (2008) 732–737, https://doi.org/10.1007/s10853-007-2178-5.
[10] M. Algarra, J. Jiménez-Jiménez, R. Moreno-Tost, B.B. Campos, J.C.G. Esteves da Silva, CdS nanocomposites assembled in porous phosphate heterostructures for fingerprint detection, Opt. Mater. (Amst) 33 (2011) 893–898, https://doi.org/10.1016/j.optmat.2011.01.017.
[11] J. Dutta, S.A. Ramakrishna, I. Mekkaoui Alaoui, Fingerprint visualization enhancement by deposition of columnar thin films and fluorescent dye treatment, Forensic Sci. Int. 228 (1-3) (2013) 32–37.
[12] M. Algarra, K. Radotić, A. Kalauzi, D. Mutavdžić, A. Savić, J. Jiménez-Jiménez, E. Rodríguez-Castellón, J.C.G.E. da Silva, J.J. Guerrero-González, Fingerprint detection and using intercalated CdSe nanoparticles on non-porous surfaces, Anal. Chim. Acta. 812 (2014) 228–235, https://doi.org/10.1016/j.aca.2014.01.015.
[13] P. Wu, C. Xu, X. Hou, J.-J. Xu, H.-Y. Chen, Dual-emitting quantum dot nanohybrid for imaging of latent fingerprints: simultaneous identification of individuals and traffic light-type visualization of TNT, Chem. Sci. 6 (2015) 4445–4450, https://doi.org/10.1039/C5SC01497B.
[14] K. Cai, R. Yang, Y. Wang, X. Yu, J. Liu, Super fast detection of latent fingerprints with water soluble CdTe quantum dots, Forensic Sci. Int. 226 (2013) 240–243, https://doi.org/10.1016/j.forsciint.2013.01.035.
[15] J. Liu, Z. Shi, Y. Yu, R. Yang, S. Zuo, Water-soluble multicolored fluorescent CdTe quantum dots: Synthesis and application for fingerprint developing, J. Colloid Interface Sci. 342 (2010) 278–282, https://doi.org/10.1016/j.jcis.2009.10.061.
[16] M. Wang, M. Li, A. Yu, J. Wu, C. Mao, Rare Earth Fluorescent Nanomaterials for Enhanced Development of Latent Fingerprints, ACS Appl. Mater. Interfaces. 7 (2015) 28110–28115, https://doi.org/10.1021/acsami.5b09320.
[17] N.M. Maalej, A. Qurashi, I. Bennour, L.R. Haddada, M.N. Shaikh, M. Ilyas, N. Essoukri Ben Amara, R. Maalej, M.A. Gondal, Green Emitting Rare Earth Gd_2O_3: Tb^{3+} Nanoparticles for Rapid Imaging of Latent Fingerprint, Methods Appl. Fluoresc. 9 (2021) 025002. https://doi.org/10.1088/2050-6120/abdbc0.
[18] X. Wang, L. Yan, S. Liu, P. Zhang, R. Huang, B. Zhou, Enhancing energy migration upconversion through a migratory interlayer in the core–shell–shell nanostructure towards latent fingerprinting, Nanoscale. 12 (2020) 18807–18814, https://doi.org/10.1039/D0NR03817B.
[19] Y. Yang, X. Liu, Y. Lu, L. Tang, J. Zhang, L. Ge, F. Li, Visualization of latent fingerprints using a simple "silver imaging ink", Anal. Methods. 8 (2016) 6293–6297, https://doi.org/10.1039/C6AY01811D.
[20] Y.-H. Cheng, Y. Zhang, S.-L. Chau, S.-K.-M. Lai, H.-W. Tang, K.-M. Ng, Enhancement of Image Contrast, Stability, and SALDI-MS Detection Sensitivity for Latent Fingerprint Analysis by Tuning the Composition of Silver-Gold Nanoalloys, ACS Appl. Mater. Interfaces. 8 (2016) 29668–29675, https://doi.org/10.1021/acsami.6b09668.
[21] G. Kolhatkar, C. Parisien, A. Ruediger, C. Muehlethaler, Latent Fingermark Imaging by Single-Metal Deposition of Gold Nanoparticles and Surface Enhanced Raman Spectroscopy, Front. Chem. 7 (2019) 440, https://doi.org/10.3389/fchem.2019.00440.
[22] I. Milenkovic, M. Algarra, C. Alcoholado, M. Cifuentes, J.M. Lázaro-Martínez, E. Rodríguez-Castellón, D. Mutavdžić, K. Radotić, T.J. Bandosz, Fingerprint imaging using N-doped carbon dots, Carbon N. Y. 144 (2019) 791–797, https://doi.org/10.1016/j.carbon.2018.12.102.
[23] D. Fernandes, M.J. Krysmann, A. Kelarakis, Carbogenically coated silica nanoparticles and their forensic applications, Chem. Commun. 52 (2016) 8294–8296, https://doi.org/10.1039/C6CC02556K.
[24] M. Algarra, D. Bartolić, K. Radotić, D. Mutavdžić, M.S. Pino-González, E. Rodríguez-Castellón, J.M. Lázaro-Martínez, J.J. Guerrero-González, J. C. Esteves da Silva, J. Jiménez-Jiménez, P-doped carbon nano-powders for fingerprint imaging, Talanta 194 (2019) 150–157, https://doi.org/10.1016/j.talanta.2018.10.033.
[25] E. Prabakaran, K. Pillay, Synthesis and characterization of fluorescent N-CDs/ZnONPs nanocomposite for latent fingerprint detection by using powder brushing method, Arab. J. Chem. 13 (2020) 3817–3835, https://doi.org/10.1016/j.arabjc.2019.01.004.
[26] F. Wang, W.B. Tan, Y. Zhang, X. Fan, M. Wang, Luminescent nanomaterials for biological labelling, Nanotechnology. 17 (2006) R1–R13, https://doi.org/10.1088/0957-4484/17/1/R01.
[27] M. Vallet-Regí, J.M. González-Calbet, Calcium phosphates as substitution of bone tissues, Prog. Solid State Chem. 32 (2004) 1–31, https://doi.org/10.1016/j.progsolidstchem.2004.07.001.
[28] K. Lin, C. Wu, J. Chang, Advances in synthesis of calcium phosphate crystals with controlled size and shape, Acta Biomater. 10 (2014) 4071–4102, https://doi.org/10.1016/j.actbio.2014.06.017.
[29] C. Qi, J. Lin, L.H. Fu, P. Huang, Calcium-based biomaterials for diagnosis, treatment, and theranostics, Chem. Soc. Rev. 47 (2018) 357–403, https://doi.org/10.1039/c6cs00746e.
[30] S.S. Syamchand, G. Sony, Multifunctional hydroxyapatite nanoparticles for drug delivery and multimodal molecular imaging, Microchim. Acta. 182 (2015) 1567–1589, https://doi.org/10.1007/s00604-015-1504-x.
[31] C. Zollfrank, L. Müller, P. Greil, F.A. Müller, Photoluminescence of annealed biomimetic apatites, Acta Biomater. 1 (2005) 663–669, https://doi.org/10.1016/j.actbio.2005.06.004.
[32] D. Aronov, A. Karlov, G. Rosenman, Hydroxyapatite nanoceramics: Basic physical properties and biointerface modification, J. Eur. Ceram. Soc. 27 (2007) 4181–4186, https://doi.org/10.1016/j.jeurceramsoc.2007.02.121.
[33] D. Aronov, M. Chaikina, J. Haddad, A. Karlov, G. Mezinskis, L. Oster, I. Pavlovska, G. Rosenman, Electronic states spectroscopy of Hydroxyapatite ceramics, J. Mater. Sci. Mater. Med. 18 (2007) 865–870, https://doi.org/10.1007/s10856-006-0080-3.
[34] C. Zhang, J. Yang, Z. Quan, P. Yang, C. Li, Z. Hou, J. Lin, Hydroxyapatite nano- and microcrystals with multiform morphologies: Controllable synthesis and luminescence properties, Cryst. Growth Des. 9 (2009) 2725–2733, https://doi.org/10.1021/cg801353n.
[35] A.V. Bystrova, Y.D. Dekhtyar, A.I. Popov, J. Coutinho, V.S. Bystrov, Modified hydroxyapatite structure and properties: Modeling and synchrotron data analysis of modified hydroxyapatite structure, Ferroelectrics 475 (2015) 135–147, https://doi.org/10.1080/00150193.2015.995580.
[36] T.R. Machado, J.C. Sczancoski, H. Beltrán-Mir, I.C. Nogueira, M.S. Li, J. Andrés, E. Cordoncillo, E. Longo, A novel approach to obtain highly intense self-activated photoluminescence emissions in hydroxyapatite nanoparticles, J. Solid State Chem. 249 (2017) 64–69, https://doi.org/10.1016/j.jssc.2016.12.018.
[37] T.R. Machado, J.C. Sczancoski, H. Beltrán-Mir, M.S. Li, J. Andrés, E. Cordoncillo, E. Leite, E. Longo, Structural properties and self-activated photoluminescence emissions in hydroxyapatite with distinct particle shapes, Ceram. Int. 44 (2018) 236–245, https://doi.org/10.1016/j.ceramint.2017.09.164.
[38] D.L. Goloshchapov, P.V. Seredin, D.A. Minakov, E.P. Domashevskaya, Photoluminescence Properties of Nanoporous Nanocrystalline Carbonate-Substituted Hydroxyapatite, Opt. Spectrosc. (English Transl. Opt. i Spektrosk. 124 (2018) 187–192, https://doi.org/10.1134/S0030400X18020066.
[39] G. Gonzalez, C. Costa-Vera, L.J. Borrero, D. Soto, L. Lozada, J.I. Chango, J.C. Diaz, L. Lascano, Effect of carbonates on hydroxyapatite self-activated photoluminescence response, J. Lumin. 195 (2018) 385–395, https://doi.org/10.1016/j.jlumin.2017.11.058.
[40] V.J. Huerta, P. Fernández, V. Gómez, O.A. Graeve, M. Herrera, Defect-related luminescence properties of hydroxyapatite nanobelts, Appl. Mater. Today. 21 (2020), 100822, https://doi.org/10.1016/j.apmt.2020.100822.
[41] E.X. Figueroa-Rosales, J. Martínez-Juárez, E. García-Díaz, D. Hernández-Cruz, S. A. Sabinas-Hernández, M.J. Robles-Águila, Photoluminescent properties of hydroxyapatite and hydroxyapatite/multi-walled carbon nanotube composites, Crystals. 11 (2021) 832, https://doi.org/10.3390/cryst11070832.
[42] A. Sinha, A. Pal, A. Santra, S. Murmu, U.K. Ghorai, A.R. Chowdhury, D. Banerjee, Calcination Temperature-Dependent Structural and Photoluminescence Properties of Hydroxyapatite Derived from Labeo Rohita Fish Scales, J. Inst. Eng. Ser. D. 101 (2) (2020) 223–232.
[43] C. Zhang, C. Li, S. Huang, Z. Hou, Z. Cheng, P. Yang, C. Peng, J. Lin, Self-activated luminescent and mesoporous strontium hydroxyapatite nanorods for drug delivery, Biomaterials 31 (2010) 3374–3383, https://doi.org/10.1016/j.biomaterials.2010.01.044.
[44] Z. Li, Z. Liu, M. Yin, X. Yang, Q. Yuan, J. Ren, X. Qu, Aptamer-capped multifunctional mesoporous strontium hydroxyapatite nanovehicle for cancer-cell-responsive drug delivery and imaging, Biomacromolecules 13 (2012) 4257–4263, https://doi.org/10.1021/bm301563q.
[45] G.S. Kumar, E.K. Girija, Flower-like hydroxyapatite nanostructure obtained from eggshell: A candidate for biomedical applications, Ceram. Int. 39 (2013) 8293–8299, https://doi.org/10.1016/j.ceramint.2013.03.099.
[46] R.K. Singh, T.H. Kim, K.D. Patel, J.J. Kim, H.W. Kim, Development of biocompatible apatite nanorod-based drug-delivery system with in situ fluorescence imaging capacity, J. Mater. Chem. B. 2 (2014) 2039–2050, https://doi.org/10.1039/c3tb21156h.
[47] S.Y. Park, K. Il Kim, S.P. Park, J.H. Lee, H.S. Jung, Aspartic Acid-Assisted Synthesis of Multifunctional Strontium-Substituted Hydroxyapatite Microspheres, Cryst. Growth Des. 16 (2016) 4318–4326, https://doi.org/10.1021/acs.cgd.6b00420.
[48] K. Deshmukh, M.M. Shaik, S.R. Ramanan, M. Kowshik, Self-Activated Fluorescent Hydroxyapatite Nanoparticles: A Promising Agent for Bioimaging and Biolabeling, ACS Biomater. Sci. Eng. 2 (2016) 1257–1264, https://doi.org/10.1021/acsbiomaterials.6b00169.
[49] T.R. Machado, I.S. Leite, N.M. Inada, M.S. Li, J.S. da Silva, J. Andrés, H. Beltrán-Mir, E. Cordoncillo, E. Longo, Designing biocompatible and multicolor fluorescent hydroxyapatite nanoparticles for cell-imaging applications, Mater. Today Chem. 14 (2019), 100211, https://doi.org/10.1016/j.mtchem.2019.100211.
[50] C. Wang, K.-J. Jeong, J. Kim, S.W. Kang, J. Kang, I.H. Han, I.-W. Lee, S.-J. Oh, J. Lee, Emission-tunable probes using terbium(III)-doped self-activated luminescent hydroxyapatite for in vitro bioimaging, J. Colloid Interface Sci. 581 (2021) 21–30, https://doi.org/10.1016/j.jcis.2020.07.083.
[51] K. Zhang, K. Zeng, C. Shen, S. Tian, M. Yang, Determination of protein kinase A activity and inhibition by using hydroxyapatite nanoparticles as a fluorescent

probe, Microchim. Acta. 185 (2018), https://doi.org/10.1007/s00604-018-2754-1.
[52] W. Yang, J. Luo, M. Qi, M. Yang, Detection of alkaline phosphatase activity and inhibition with fluorescent hydroxyapatite nanoparticles, Anal. Methods. 11 (2019) 2272–2276, https://doi.org/10.1039/c9ay00176j.
[53] C. Cheng, K. Tong, Y. Fang, J. Wang, Y. Liu, J. Tan, Ammonium-induced synthesis of highly fluorescent hydroxyapatite nanoparticles with excellent aqueous colloidal stability for secure information storage, Coatings. 9 (2019) 1–14, https://doi.org/10.3390/coatings9050289.
[54] V.S. Bystrov, C. Piccirillo, D.M. Tobaldi, P.M.L. Castro, J. Coutinho, S. Kopyl, R. C. Pullar, Oxygen vacancies, the optical band gap (Eg) and photocatalysis of hydroxyapatite: Comparing modelling with measured data, Appl. Catal. B Environ. 196 (2016) 100–107, https://doi.org/10.1016/j.apcatb.2016.05.014.
[55] G. Lambrecht, C. Mallol, Autofluorescence of experimentally heated bone: Potential archaeological applications and relevance for estimating degree of burning, J. Archaeol. Sci. Reports. 31 (2020), 102333, https://doi.org/10.1016/j.jasrep.2020.102333.
[56] A. Sandri, P.R. Basso, I. Corridori, M. Protasoni, G. Segalla, M. Raspanti, A. E. Spinelli, F. Boschi, Photon emission and changes in fluorescent properties of bone after laser irradiation, J. Biophotonics. 14 (2021) 1–9, https://doi.org/10.1002/jbio.202000445.
[57] D.L. Goloshchapov, D.A. Minakov, E.P. Domashevskaya, P.V. Seredin, Excitation of luminescence of the nanoporous bioactive nanocrystalline carbonate-substituted hydroxyapatite for early tooth disease detection, Results Phys. 7 (2017) 3853–3858, https://doi.org/10.1016/j.rinp.2017.09.055.
[58] S.V. Dorozhkin, Amorphous calcium (ortho)phosphates, Acta Biomater. 6 (2010) 4457–4475, https://doi.org/10.1016/j.actbio.2010.06.031.
[59] C. Combes, C. Rey, Amorphous calcium phosphates: Synthesis, properties and uses in biomaterials, Acta Biomater. 6 (2010) 3362–3378, https://doi.org/10.1016/j.actbio.2010.02.017.
[60] V. Uskoković, Disordering the Disorder as the Route to a Higher Order: Incoherent Crystallization of Calcium Phosphate through Amorphous Precursors, Cryst. Growth Des. 19 (2019) 4340–4357, https://doi.org/10.1021/acs.cgd.9b00061.
[61] V. Uskoković, S. Marković, L. Veselinović, S. Škapin, N. Ignjatović, D. P. Uskoković, Insights into the kinetics of thermally induced crystallization of amorphous calcium phosphate, Phys. Chem. Chem. Phys. 20 (2018) 29221–29235, https://doi.org/10.1039/c8cp06460a.
[62] O.F. Yasar, W.C. Liao, B. Stevensson, M. Edén, Structural Role and Spatial Distribution of Carbonate Ions in Amorphous Calcium Phosphate, J. Phys. Chem. C. 125 (2021) 4675–4693, https://doi.org/10.1021/acs.jpcc.0c10355.
[63] M. Edén, Structure and formation of amorphous calcium phosphate and its role as surface layer of nanocrystalline apatite: Implications for bone mineralization, Materialia. 17 (2021), 101107, https://doi.org/10.1016/j.mtla.2021.101107.
[64] S.V. Dorozhkin, Synthetic amorphous calcium phosphates (ACPs): Preparation, structure, properties, and biomedical applications, Biomater. Sci. 9 (2021) 7748–7798, https://doi.org/10.1039/d1bm01239h.
[65] A.S. Posner, F. Betts, Synthetic Amorphous Calcium Phosphate and Its Relation to Bone Mineral Structure, Acc. Chem. Res. 8 (8) (1975) 273–281.
[66] S. Somrani, M. Banu, M. Jemal, C. Rey, Physico-chemical and thermochemical studies of the hydrolytic conversion of amorphous tricalcium phosphate into apatite, J. Solid State Chem. 178 (2005) 1337–1348, https://doi.org/10.1016/j.jssc.2004.11.029.
[67] E.D. Eanes, Thermochemical studies on amorphous calcium phosphate, Calcif. Tissue Res. 5 (1970) 133–145, https://doi.org/10.1007/BF02017543.
[68] N. Li, W. Cui, P. Cong, J. Tang, Y. Guan, C. Huang, Y. Liu, C. Yu, R. Yang, X. Zhang, Biomimetic inorganic-organic hybrid nanoparticles from magnesium-substituted amorphous calcium phosphate clusters and polyacrylic acid molecules, Bioact. Mater. 6 (2021) 2303–2314, https://doi.org/10.1016/j.bioactmat.2021.01.005.
[69] J.D. Termine, D.R. Lundy, Vibrational spectra of some phosphate salts amorphous to X-ray diffraction, Calcif. Tissue Res. 15 (1974) 55–70, https://doi.org/10.1007/BF02059043.
[70] S.J. Gadaleta, E.P. Paschalis, F. Betts, R. Mendelsohn, A.L. Boskey, Fourier transform infrared spectroscopy of the solution-mediated conversion of amorphous calcium phosphate to hydroxyapatite: New correlations between X-ray diffraction and infrared data, Calcif. Tissue Int. 58 (1996) 9–16, https://doi.org/10.1007/BF02509540.
[71] D. Tadic, F. Peters, M. Epple, Continuous synthesis of amorphous carbonated apatites, Biomaterials 23 (2002) 2553–2559, https://doi.org/10.1016/S0142-9612(01)00390-8.
[72] P. Layrolle, A. Lebugle, Characterization and Reactivity of Nanosized Calcium Phosphates Prepared in Anhydrous Ethanol, Chem. Mater. 6 (1994) 1996–2004, https://doi.org/10.1021/cm00047a019.
[73] J. Vecstaudza, M. Gasik, J. Locs, Amorphous calcium phosphate materials: Formation, structure and thermal behaviour, J. Eur. Ceram. Soc. 39 (2019) 1642–1649, https://doi.org/10.1016/j.jeurceramsoc.2018.11.003.
[74] P.C.H. Mitchell, S.F. Parker, K. Simkiss, J. Simmons, M.G. Taylor, Hydrated sites in biogenic amorphous calcium phosphates: An infrared, Raman, and inelastic neutron scattering study, J. Inorg. Biochem. 62 (1996) 183–197, https://doi.org/10.1016/0162-0134(95)00146-8.
[75] J.M. Holmes, R.A. Beebe, Surface areas by gas adsorption on amorphous calcium phosphate and crystalline hydroxyapatite, Calcif. Tissue Res. 7 (1971) 163–174, https://doi.org/10.1007/BF02062604.
[76] J.D. Termine, E.D. Eanes, Comparative chemistry of amorphous and apatitic calcium phosphate preparations, Calcif. Tissue Res. 10 (1972) 171–197, https://doi.org/10.1007/BF02012548.
[77] G. Montes-Hernandez, F. Renard, Nucleation of Brushite and Hydroxyapatite from Amorphous Calcium Phosphate Phases Revealed by Dynamic in Situ Raman Spectroscopy, J. Phys. Chem. C. 124 (2020) 15302–15311, https://doi.org/10.1021/acs.jpcc.0c04028.
[78] M. Fleet, Carbonated hydroxyapatite: Materials, synthesis, and applications (2014).
[79] T. Theophanides, Infrared spectroscopy - Materials Science, Eng. Technol. (2012).
[80] D. Stoilova, V. Koleva, V. Vassileva, Infrared study of some synthetic phases of malachite ($Cu_2(OH)_2CO_3$)-hydrozincite ($Zn_5(OH)_6(CO_3)_2$) series, Spectrochim. Acta - Part A Mol, Biomol. Spectrosc. 58 (9) (2002) 2051–2059.
[81] J.E. Amonette, D. Rai, Identification of noncrystalline (Fe, Cr)($OH_3$3 by infrared spectroscopy, Clays Clay Miner. 38 (1990) 129–136.
[82] J.P. Jolivet, Y. Thomas, B. Taravel, V. Lorenzelli, G. Busca, Infrared spectra of cerium and thorium pentacarbonate complexes, J. Mol. Struct. 79 (1982) 403–408, https://doi.org/10.1016/0022-2860(82)85091-6.
[83] J.F. Moulder, W.F. Stickle, P.E. Sobol, K.D. Bomben, Handbook of X-ray photoelectron spectroscopy: A reference book of standard spectra for identification and interpretation of XPS, Data (1995).
[84] V. Bemmer, M. Bowker, J.H. Carter, P.R. Davies, L.E. Edwards, K.D.M. Harris, C. E. Hughes, F. Robinson, D.J. Morgan, M.G. Thomas, Rationalization of the X-ray photoelectron spectroscopy of aluminium phosphates synthesized from different precursors, RSC Adv. 10 (14) (2020) 8444–8452.
[85] S. Kasap, P. Capper, Springer handbook of electronic and photonic materials, 2nd edition, Springer International Publishing, Gewerbestrasse, Switzerland, 2017. https://doi.org/10.1007/978-3-319-48933-9_39.
[86] Z. Chen, H.N. Dinh, E. Miller, Photoelectrochemical Water Splitting: Standards, Experimental Methodos, and Protocols, Springer-Verlag, New York (2013), https://doi.org/10.1016/B978-0-12-814134-2.00028-0.
[87] P. Makuła, M. Pacia, W. Macyk, How To Correctly Determine the Band Gap Energy of Modified Semiconductor Photocatalysts Based on UV-Vis Spectra, J. Phys. Chem. Lett. 9 (2018) 6814–6817, https://doi.org/10.1021/acs.jpclett.8b02892.
[88] L. Liang, P. Rulis, W.Y. Ching, Mechanical properties, electronic structure and bonding of α-and β-tricalcium phosphates with surface characterization, Acta Biomater. 6 (2010) 3763–3771, https://doi.org/10.1016/j.actbio.2010.03.033.
[89] P. Rulis, L. Ouyang, W.Y. Ching, Electronic structure and bonding in calcium apatite crystals: Hydroxyapatite, fluorapatite, chlorapatite, and bromapatite, Phys. Rev. B - Condens. Matter Mater. Phys. 70 (2004) 1–8, https://doi.org/10.1103/PhysRevB.70.155104.
[90] A. Slepko, A.A. Demkov, First-principles study of the biomineral hydroxyapatite, Phys. Rev. B - Condens. Matter Mater. Phys. 84 (2011) 1–11, https://doi.org/10.1103/PhysRevB.84.134108.
[91] M.E. Zilm, L. Chen, V. Sharma, A. McDannald, M. Jain, R. Ramprasad, M. Wei, Hydroxyapatite substituted by transition metals: Experiment and theory, Phys. Chem. Chem. Phys. 18 (2016) 16457–16465, https://doi.org/10.1039/c6cp00474a.
[92] Y. Jiménez-Flores, M. Suárez-Quezada, J.B. Rojas-Trigos, L. Lartundo-Rojas, V. Suárez, A. Mantilla, Characterization of Tb-doped hydroxyapatite for biomedical applications: optical properties and energy band gap determination, J. Mater. Sci. 52 (2017) 9990–10000, https://doi.org/10.1007/s10853-017-1201-8.
[93] N.L. Ignjatović, L. Mančić, M. Vuković, Z. Stojanović, M.G. Nikolić, S. Škapin, S. Jovanović, L. Veselinović, V. Uskoković, S. Lazić, S. Marković, M.M. Lazarević, D.P. Uskoković, Rare-earth (Gd^{3+}, $Y^{b3}+/T^{m3}+$, $E^{u3}+$) co-doped hydroxyapatite as magnetic, up-conversion and down-conversion materials for multimodal imaging, Sci. Rep. 9 (2019) 1–15, https://doi.org/10.1038/s41598-019-52885-0.
[94] S.S. Bhat, U.V. Waghmare, U. Ramamurty, First-principles study of structure, vibrational, and elastic properties of stoichiometric and calcium-deficient hydroxyapatite, Cryst. Growth Des. 14 (2014) 3131–3141, https://doi.org/10.1021/cg5004269.
[95] B. Goswami, A. Choudhury, Enhanced visible luminescence and modification in morphological properties of cadmium oxide nanoparticles induced by annealing, J. Exp. Nanosci. 10 (2015) 900–910, https://doi.org/10.1080/17458080.2014.933492.
[96] E. Cerrato, M.C. Paganini, E. Giamello, Photoactivity under visible light of defective ZnO investigated by EPR spectroscopy and photoluminescence, J. Photochem. Photobiol. A Chem. 397 (2020), 112531, https://doi.org/10.1016/j.jphotochem.2020.112531.
[97] E.R. Leite, F.M. Pontes, E.C. Paris, C.A. Paskocimas, E.J.H. Lee, E. Longo, P. S. Pizani, J.A. Varela, V. Mastelaro, Amorphous lead titanate: A new wide-band gap semiconductor with photoluminescence at room temperature, Adv. Funct. Mater. 10 (2000) 235–240, https://doi.org/10.1002/1099-0712(200011/12)10:6<235::AID-AMO409>3.0.CO;2-6.
[98] E. Orhan, M. Anicete-Santos, M.A.M.A. Maurera, F.M. Pontes, C.O. Paiva-Santos, A.G. Souza, J.A. Varela, P.S. Pizani, E. Longo, Conditions giving rise to intense visible room temperature photoluminescence in $SrWO_4$ thin films: The role of disorder, Chem. Phys. 312 (2005) 1–9, https://doi.org/10.1016/j.chemphys.2004.11.013.
[99] M. Anicete-Santos, M.S. Silva, E. Orhan, M.S. Góes, M.A. Zaghete, C.O. Paiva-Santos, P.S. Pizani, M. Cilense, J.A. Varela, E. Longo, Contribution of structural order-disorder to the room-temperature photoluminescence of lead zirconate titanate powders, J. Lumin. 127 (2007) 689–695, https://doi.org/10.1016/j.jlumin.2007.04.002.

[100] V. Uskoković, D.P. Uskoković, Nanosized hydroxyapatite and other calcium phosphates: Chemistry of formation and application as drug and gene delivery agents, J. Biomed. Mater. Res. 96B (1) (2011) 152–191.
[101] K. Onuma, A. Ito, Cluster Growth Model for Hydroxyapatite, Chem. Mater. 10 (1998) 3346–3351, https://doi.org/10.1021/cm980062c.
[102] A. Lotsari, A.K. Rajasekharan, M. Halvarsson, M. Andersson, Transformation of amorphous calcium phosphate to bone-like apatite, Nat. Commun. 9 (2018) 4170, https://doi.org/10.1038/s41467-018-06570-x.
[103] K. Matsunaga, A. Kuwabara, First-principles study of vacancy formation in hydroxyapatite, Phys. Rev. B - Condens. Matter Mater. Phys. 75 (2007) 1–9, https://doi.org/10.1103/PhysRevB.75.014102.
[104] V.S. Bystrov, J. Coutinho, A.V. Bystrova, Y.D. Dekhtyar, R.C. Pullar, A. Poronin, E. Palcevskis, A. Dindune, B. Alkan, C. Durucan, E.V. Paramonova, Computational study of hydroxyapatite structures, properties and defects, J. Phys. D. Appl. Phys. 48 (19) (2015) 195302.
[105] D. Jiang, H. Zhao, Y. Yang, Y. Zhu, X. Chen, J. Sun, K. Yu, H. Fan, X. Zhang, Investigation of luminescent mechanism: N-rich carbon dots as luminescence centers in fluorescent hydroxyapatite prepared using a typical hydrothermal process, J. Mater. Chem. B. 5 (2017) 3749–3757, https://doi.org/10.1039/c6tb03184f.
[106] V. Uskoković, X-ray photoelectron and ion scattering spectroscopic surface analyses of amorphous and crystalline calcium phosphate nanoparticles with different chemical histories, Phys. Chem. Chem. Phys. 22 (2020) 5531–5547, https://doi.org/10.1039/c9cp06529f.
[107] L.W. Du, S. Bian, B. Di Gou, Y. Jiang, J. Huang, Y.X. Gao, Y.D. Zhao, W. Wen, T. L. Zhang, K. Wang, Structure of clusters and formation of amorphous calcium phosphate and hydroxyapatite: From the perspective of coordination chemistry, Cryst. Growth Des. 13 (2013) 3103–3109, https://doi.org/10.1021/cg400498j.
[108] P. Yang, Z. Quan, C. Li, X. Kang, H. Lian, J. Lin, Bioactive, luminescent and mesoporous europium-doped hydroxyapatite as a drug carrier, Biomaterials 29 (2008) 4341–4347, https://doi.org/10.1016/j.biomaterials.2008.07.042.
[109] J. Hui, X. Zhang, Z. Zhang, S. Wang, L. Tao, Y. Wei, X. Wang, Fluoridated HAp:Ln^{3+} (Ln = Eu or Tb) nanoparticles for cell-imaging, Nanoscale. 4 (2012) 6967–6970, https://doi.org/10.1039/c2nr32404k.
[110] Y. Xie, W. He, F. Li, T.S.H. Perera, L. Gan, Y. Han, X. Wang, S. Li, H. Dai, Luminescence Enhanced Eu^{3+}/Gd^{3+} Co-Doped Hydroxyapatite Nanocrystals as Imaging Agents in Vitro and in Vivo, ACS Appl. Mater. Interfaces. 8 (2016) 10212–10219, https://doi.org/10.1021/acsami.6b01814.
[111] H.N. Van, P.D. Tam, N.D.T. Kien, P.T. Huy, V.-H. Pham, Enhancing the luminescence of Eu 3+ /Eu 2+ ion-doped hydroxyapatite by fluoridation and thermal annealing : fluor-hydroxyapatite; luminescence; europium, nanobiophosphors, Luminescence 32 (5) (2017) 817–823.
[112] K. Carrera, V. Huerta, V. Orozco, J. Matutes, P. Fernández, O.A. Graeve, M. Herrera, Formation of vacancy point-defects in hydroxyapatite nanobelts by selective incorporation of Fe^{3+} ions in Ca(II) sites. A CL and XPS study, Mater. Sci. Eng. B Solid-State Mater. Adv. Technol. 271 (2021) 115308.
[113] S.S. Nadar, R.K. Kelkar, P.V. Pise, N.P. Patil, S.P. Patil, N.S. Chaubal-Durve, V. P. Bhange, M.S. Tiwari, P.D. Patil, The untapped potential of magnetic nanoparticles for forensic investigations: A comprehensive review, Talanta 230 (2021), 122297, https://doi.org/10.1016/j.talanta.2021.122297.
[114] N. Attard Montalto, J.J. Ojeda, B.J. Jones, Determining the order of deposition of natural latent fingerprints and laser printed ink using chemical mapping with secondary ion mass spectrometry, Sci. Justice. 53 (2013) 2–7, https://doi.org/10.1016/j.scijus.2012.05.007.
[115] M.W. Mofulatsi, E. Prabakaran, T. Velempini, E. Green, K. Pillay, Preparation of manganese oxide coated coal fly ash adsorbent for the removal of lead and reuse for latent fingerprint detection, Microporous Mesoporous Mater. 329 (2022), 111480, https://doi.org/10.1016/j.micromeso.2021.111480.